Bioorganic & Medicinal Chemistry 20 (2012) 7194–7205

Contents lists available at SciVerse ScienceDirect

Bioorganic & Medicinal Chemistry

journal homepage: www.elsevier.com/locate/bmc

# Influence of thiostrepton binding on the ribosomal GTPase associated region characterized by molecular dynamics simulation

Antje Wolf [a,b], Sascha Baumann [c,d], Hans-Dieter Arndt [c,e], Karl N. Kirschner [f,*]

[a] Department of Bioinformatics, Fraunhofer-Institute for Algorithms and Scientific Computing (SCAI), Schloss Birlinghoven, 53754 Sankt Augustin, Germany
[b] Department of Life Science Informatics, B-IT, Rheinische Friedrich-Wilhelms-Universität, Dahlmannstr. 2, 53113 Bonn, Germany
[c] Max-Planck-Institute of Molecular Physiology, Otto-Hahn-Strasse 11, 44227 Dortmund, Germany
[d] Technische Universität Dortmund, Faculty of Chemistry, Otto-Hahn-Strasse 6, 44221 Dortmund, Germany
[e] Friedrich-Schiller Universität, Institute of Organic and Macromolecular Chemistry, Humboldtstr. 10, 07743 Jena, Germany
[f] Department of Simulation Engineering, Fraunhofer-Institute for Algorithms and Scientific Computing (SCAI), Schloss Birlinghoven, 53754 Sankt Augustin, Germany

ARTICLE INFO

*Article history:*
Received 10 July 2012
Revised 11 September 2012
Accepted 13 September 2012
Available online 22 September 2012

*Keywords:*
Ribosome
GTPase associated region (GAR)
Thiopeptide
Protein and RNA interface
Dynamics

ABSTRACT

The thiostrepton antibiotic inhibits bacterial protein synthesis by binding to a cleft formed by the ribosomal protein L11 and 23S's rRNA helices 43–44 on the 70S ribosome. It was proposed from crystal structures that the ligand restricts L11's N-terminal movement and thus prevents proper translation factor binding. An exact understanding of thiostrepton's impact on the binding site's dynamics at atomistic resolution is still missing. Here we report an all-atom molecular dynamics simulations of the binary L11 · rRNA and the ternary L11 · rRNA · thiostrepton complex (rRNA = helices 43–44). We demonstrate that thiostrepton directly impacts the binding site's atomic and biomacromolecular dynamics.



## 1. Introduction

The GTPase associated region (GAR) on the 70S ribosome plays a central role in peptide elongation by providing a docking site for elongation factors and by coordinating GTP hydrolysis during protein synthesis.[1–3] The GAR is primarily formed by the ribosomal protein L11 and the helix 43–44 (H43–H44) substructure of the 23S ribosomal RNA. L11 is a highly conserved two-domain protein, whose C-terminal domain (CTD) tightly binds to the compactly folded rRNA and orients the N-terminal domain (NTD). The NTD itself makes very limited contacts with the rRNA.[4] The detection of different NTD orientations strongly suggests that its dynamic motion is critical for function and binding with elongation and initiation factors.[5,3]

The importance of the bacterial GAR in protein synthesis, coupled with the identification of potent natural product antibiotics targeting it, renders this region an interesting target for drug development.[6] The thiopeptide antibiotic thiostrepton (TS)[7,8] inhibits bacterial protein biosynthesis by tightly binding to the cleft formed by the GAR's L11 protein and H43–H44 helices of the 23S rRNA.[9–12] This ternary binding event was shown to be highly cooperative and necessitates the presence of both rRNA and protein components. Furthermore, recent data suggest that TS binding impedes stable binding of EF-G and EF-4.[13] Interpretations of ribosomal crystal structures in the 3.2–4.2 Å resolution range have strengthened the hypothesis that TS restricts the protein's NTD movement, and thereby prevents proper binding and processing of translation factors.[14,3] However, the resistance data for thiopeptide antibiotics cannot easily be aligned with a static lock-and-key model for inhibitor binding.[15] Obtaining atomic resolution data of the L11 · 23S binding site dynamics and the effects of inhibitor binding would improve our understanding of the multifaceted interaction between ligand, protein and rRNA—and potentially guide further drug discovery.

One possible mean for acquiring such data are molecular dynamics (MD) simulations. Thereby insights into the structure and dynamics of large biomolecular complexes can be provided in silico at the atomic level that cannot be generated by other methods. When implemented and results interpreted carefully, MD simulations provide valuable qualitative and semi-quantitative information about the structure and dynamics of folded RNA molecules and protein–RNA complexes,[16–19] especially when calibrated by experimental observation. For example, simulations have revealed functionally significant stochastic fluctuations of RNA building blocks, where ribosomal kink-turns may play a role in translocation.[20,21] The intrinsic flexibility of H38[22] and the H42–H44 segment of the 23S rRNA have been described by

* Corresponding author.
*E-mail address:* karl.kirschner@scai.fraunhofer.de (K.N. Kirschner).

0968-0896/$ - see front matter © 2012 Elsevier Ltd. All rights reserved.
http://dx.doi.org/10.1016/j.bmc.2012.09.025

simulations.[23] More recent simulations on three rRNA three-way junctions demonstrated significant anisotropic hinge-like flexibility between stacked stems.[24] Whitford et al. performed an impressive 2.1 μs worth of all-atom simulations of the 70S ribosome to provide a relationship between computed free-energy profile for elbow-accommodation and its experimental kinetics.[25]

In the last decade, MD simulations of RNA–protein complexes have been enriched by the growing number of high-resolution crystal structures.[17] These works include coarse-grained[26] and all-atom[27,28] simulations of the entire ribosome, as well as simulations of diverse protein–rRNA interactions,[29–32] including the ligand-free GAR.[31] By using an MD simulation, Frank and co-workers identified two L11 conformations that matched cryo-EM maps and were interpreted as bound and unbound states to the aa–tRNA–EF–Tu–GTP ternary complex.[31] Thus, despite the ribosome's challenging size and molecular complexity, MD studies have contributed valuable insights into its functional properties.

Here we performed all-atom MD simulations of the binary L11 · rRNA complex and the ternary L11 · rRNA · TS complex (where rRNA is helix 43–44 of 23S) to investigate the ligand's binding and its influence on the dynamics of the ribosomal protein–RNA complex. We demonstrate that TS binding restricts the thermal motion of the nearby NTD, its α1-helix secondary element, and exerts weak but detectable dynamic coupling to the distant CTD. To our knowledge, this is the first reported MD study that models L11, a portion of 23S, and a natural product together, and represents the foundation for our computational drug-design research efforts involving thiopeptides.

## 2. Materials and methods

### 2.1. Biochemistry

*Escherichia coli* 23S rRNA fragments were prepared by T7 in vitro transcription and gel purified as described elsewhere.[15] The 63 nt sequence used for spectroscopy was 5′-G**GCCAGGAUG-UUGGCUUAGA-AGCAGCCAUC-AUUUAAAGAA-AGCGUAAUAG-CUCACUGGU**C-UAG-3′ (*E. coli* sequence 1051–1108 in bold). rRNA concentration was determined by absorbance measurement at 260 nM using $\varepsilon_{260} = 0.6404\,\mu mol^{-1}\,cm^{-1}$. *Thermus thermophilus* L11 protein was expressed as N-terminally $His_6$ – tagged fusion construct and purified using $Ni^{2+}$ · NTA affinity chromatography.[15] Protein concentrations were determined by absorbance measurement at 280 nM using computed extinction coefficients.[33] Thiostrepton was obtained from Calbiochem and used directly (HPLC purity > 95%). TS stock solutions (100×) were prepared in trifluoroethanol (TFE). Ligand concentrations were determined by absorbance measurement at 280 nM using $\varepsilon_{280} = 0.027\,\mu mol^{-1}\,cm^{-1}$.[34]

### 2.2. CD-spectroscopy

All samples were prepared in 25 mM $Na_2HPO_4/NaH_2PO_4$ buffer (pH 8.0) supplemented with 10 mM $MgCl_2$, containing 1% TFE (v/v). CD-spectra were recorded on a J-815 spectrometer (Jasco Deutschland GmbH, Gross-Umstadt, Germany) at 5 °C (0.5 nm steps, continuous mode, 0.5 nm bandwidth, scan rate 100 nm/min) using quartz cuvettes ($d = 2$ mm). The spectra were analyzed using the Jasco Spectra Manager software package (V1.0). Spectral signatures were invariant to the presence of the $His_6$ – tag and to the presence of TFE in the medium (up to 5%).

For the CD titrations constant concentration of the 23S RNA fragment (2 μM) or L11 (3 μM) alone, as well as equimolar mixtures of the 23S RNA fragments and L11 (2 μM), were mixed with varying TS concentrations and incubated for 1 h at 5 °C. The CD-spectra of varying concentrations of TS without RNA or protein were recorded for comparison. For each sample the averaged CD-spectral sum (10 accumulations) was recorded from 350 to 200 nm. The free ligand TS displayed a very weak CD-signature only detectable at concentrations > 6 μM with two major peaks at 210 and 250 nm, respectively (Supplementary Figure. 1). Interference with the strong signals from RNA or protein could hence be excluded.

### 2.3. Molecular dynamics simulations

To construct the computational models, the crystal coordinates (PDB code 3CF5)[14] of the TS-bound 50S subunit from *Deinococcus radiodurans* were used. Only the atoms associated with the L11 protein, with helices H43–H44 of the 23S rRNA (i.e., residues 1051–1108), and of TS were extracted. For the simulation without ligand, the resulting vacancy was filled with water. All simulations were performed using AMBER9 and 11.[35] The Parmbsc0 and Parm99SB[36] force fields[37] were used for the rRNA and protein residues. Throughout this paper the residue numbering is according to the sequence given in Ref. 14.

The TS model preparation required special consideration due to its constitution and large size. TS was separated into its constituent residues as defined by Bond et al.[38] Parameters for the standard amino acid residues were taken from the Parm99SB force field.[36] For the non-standard residues, atom-type appropriate intramolecular and Lennard-Jones parameters were taken from the General Amber Force Field (GAFF).[39] Each non-standard residue was capped using the nearest functional group present in the structure, and terminated using a methyl group—as exemplified in Figure 1. This was done to include any local electron delocalization present in the macrocycle during the determination of a residue's partial atomic charges. These residue analogues were optimized at the HF/6-31G(d) level of theory, and verified as minima using frequency analysis. Molecular electrostatic potentials were subsequently constructed using the CHELPG methodology.[40] A restrained electrostatic potential fit (i.e., RESP) was performed using a 0.01 weighting factor to obtain partial atomic charges that are compatible with Parm99SB.[41] The capping groups were subsequently removed from each residue, and the remaining residual charge were neutralized. All quantum mechanics calculations were performed using GAMESS.[42] Atom type assignment and the partial atomic charges for TS can be found in Supplementary Table 1, with corresponding atom labels is Supplementary Figure 2.

The protein–rRNA complex was neutralized using 50 sodium ions and solvated in a truncated octahedron of TIP3P[43] waters with a 15 Å padding in all directions. Our use of net-neutralizing sodium ions rather than divalent ions or experimental salt conditions follow the rationalization presented by Ŝponer and co-workers.[23] The resulting model sizes were 55,186 and 50,435 atoms for the L11 · rRNA and L11 · rRNA · TS systems. A series of minimizations were performed on the model to an energy gradient convergence of $0.6\,kcal{\cdot}mol^{-1}$. Afterwards, three sequential MD simulations were performed where the portion of allowed motion included (a) just the water molecules and sodium ions, (b) water, sodium ions, added hydrogens, and capping residues, and finally (c) the entire system. Each simulation was heated from 5 to 310 K in 100 ps and cooled back to 5 K in another 100 ps; for temperatures below 155 K the simulations were performed at a constant volume, while over 155 K the simulations were at a constant pressure of 1 bar. Finally, a constant pressure production run was conducted at 310 K without restraints. A chart describing this simulation protocol can be found in Supplementary Figure 3.

Density, volume, and energy were monitored, as appropriate for each stage, to ensure simulation stability. A cutoff of 9 Å was used, while the Particle Mesh Ewald method[44] was employed to capture the longer non-bonded interactions. Electrostatic and vdW

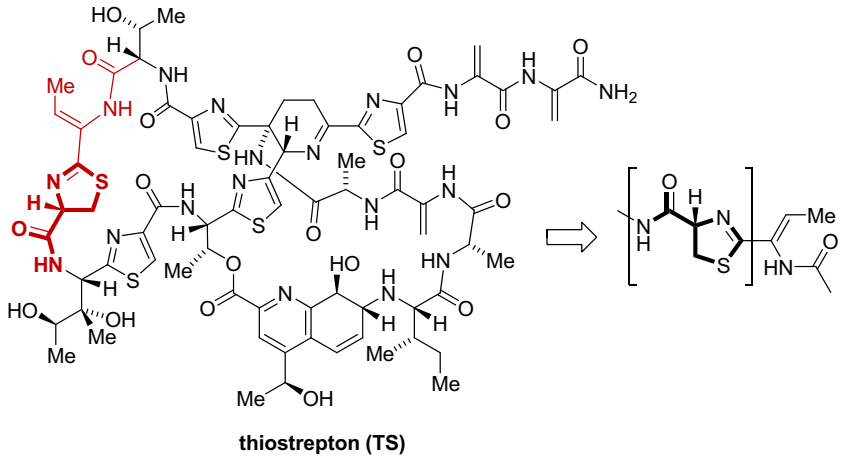


**Fig. 1.** Illustration of substructure extraction from thiostrepton (TS) and illustration of capping nonnatural amino acid residues. Such a procedure is necessary for determining TS's partial atomic charges, which is part of the ligand's force-field parameterization. In the case shown, the thiazoline-4-carboxyl residue (bracketed) is capped using the nearest functional groups of TS (dehydrobutyrine and thiostreptine).

interactions between atoms separated by three bonds were reduced by factors of 1.2 and 2.0. Temperature regulation was controlled using Langevin dynamics with a collision frequency of 1 $ps^{-1}$ and a unique random-prime-number seed was used at each restart point.[35] The SHAKE algorithm[45] was used to constrain bonds involving hydrogen atoms, and subsequently these bonds were excluded from the force evaluation. A time step of 1 fs was used during equilibration and increased to 2 fs during the production run. Coordinates were recorded every 1 ps. To help substantiate our observations, each of the two simulations was repeated for another 40 ns using the same protocol, but starting with different random number seeds, resulting in a total of 80 ns worth of data per model.

## 2.4. Analysis of MD trajectories

All analyses were performed on the trajectory data generated from the production simulations for both models. Prior to each analysis, the structures within each trajectory were aligned using the backbone atoms (i.e., Cα, C, N for the protein and P, C3′, C4′, C5′, O3′, O5′ for the rRNA) to the X-ray structure, except when stated otherwise. Such preanalysis alignment removes system-wide translational and rotational movements.

### 2.4.1. RMSD and RMSF:

The root-mean-squared deviation (RMSD) and fluctuations (RMSF) were calculated for the protein and rRNA backbone atoms using the PTRAJ module of AMBER.[35]

### 2.4.2. Cross-correlation analysis:

For the dynamic cross-correlation analysis, the covariance matrices were computed using PTRAJ. The corresponding dynamic cross-correlation maps (DCCMs) were plotted using the statistics package R (V2.10).[46]

### 2.4.3. Principal component analysis and clustering:

Principal component (PC) analysis[47,48] was done using R and the bio3d package,[49] which was developed specifically for analyzing biomolecular data. For this analysis, only Cα and P atoms were considered. The snapshots were clustered along the PC subspace spanned by the first three PCs using the K-means method, as implemented in R. (The full details of clustering the different PC subspaces can be found in Ref. 50.) The resulting clusters were mapped back onto the RMSD versus time plot to provide trajectory time-frames for cluster existence. Subsequently, the conformational representatives of each cluster were obtained by selecting the conformational snapshot with the lowest RMSD value to the cluster centroid (i.e., the average conformation).

### 2.4.4. Secondary structure:

The protein secondary structure was computed throughout each simulation using the DSSP method,[51] as implemented in PTRAJ.

### 2.4.5. rRNA conformations:

The $\chi$ – angle and sugar pucker of all nucleic acids were monitored throughout both simulations. The $\chi$ – angle was defined by the O4′ – C1′ – N9 – C4 torsion, while the sugar puckering was characterized via the pseudorotational phase angle P as defined by Altona and Sundaralingam.[52] Two additional water solvated simulations were performed on the adenosine (A) monomer and the AAA trimer, whose results were used to help validate the finding in the ribosome simulations.

## 3. Results

### 3.1. CD-spectroscopy

To identify if conformational changes occur upon ligand binding, we reconstituted the L11 · 23S *Thermus thermophilus* complex under close-to-native conditions in vitro and conducted CD titrations at low μM concentrations where TS does not precipitate.[12,34] The sole 23S rRNA fragment displayed the typical CD signature of a predominant A-form RNA helix with maxima at 210 and 265 nm (Fig. 2A).[53] Titrations of the fragment with increasing TS concentrations (up to a fivefold excess) had no detectable effect on the rRNA CD spectrum (Fig. 2A) and and hence on its overall conformation.

The *T. thermophilus* L11 protein displayed the CD signature of a predominantly $\alpha$ – helical fold with typical maxima at 200, 210, and 220 nm[53] (Fig. 2B), congruent with the available structural data of similar homologs.[14,4,5] Titrations of L11 with increasing TS concentrations (up to a twofold excess) did not affect the protein's CD spectrum. Hence the overall conformation of the isolated L11 protein remains unaffected by TS.

As expected, stoichiometric complexes of the 23S rRNA fragment and L11 showed a characteristic sum spectrum of the RNA and protein CD contributions, with RNA–protein sum maxima at 210 and 220 nm, and an RNA-derived maximum at 265 nm. In

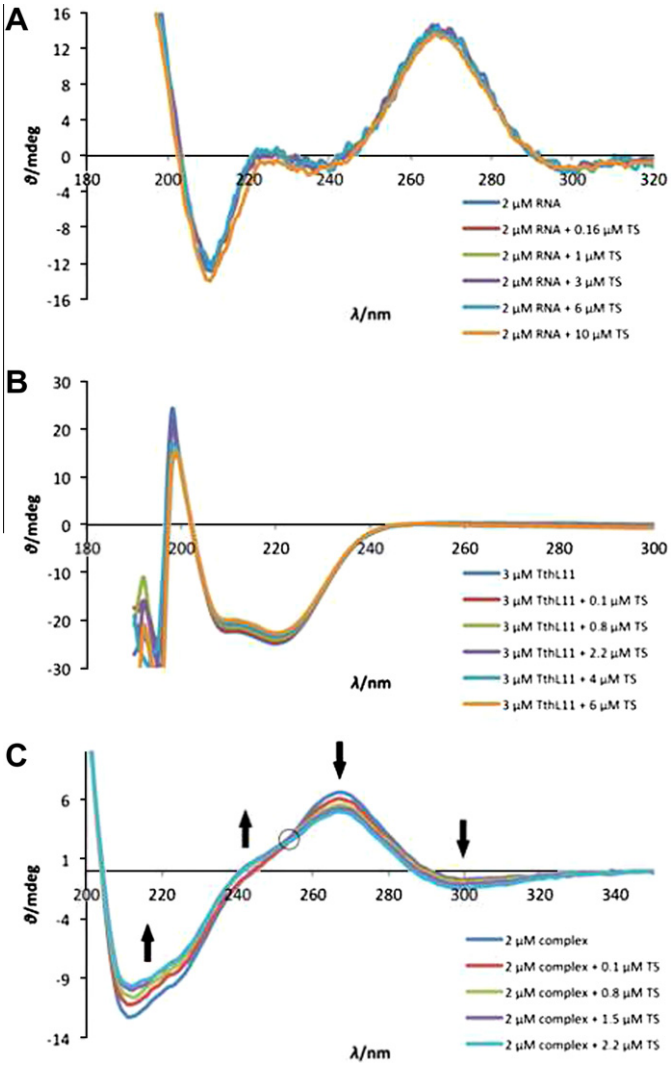


**Fig. 2.** CD titrations with TS. (A) Isolated rRNA fragment (2 μM) with 0, 0.16, 1, 3, 6, and10 μM TS; (B) isolated L11 protein (3 μM) with 0, 0.5, 0.8, 2.2, 4, and6 μM TS; (C) reconstituted L11 · 23S complex (2 μM) with 0.1, 0.8, 1.5, and2.2 μM TS. Filled arrows indicate characteristic band shifts upon increasing ligand concentration. Circle marks isosbestic point at 254 nM.

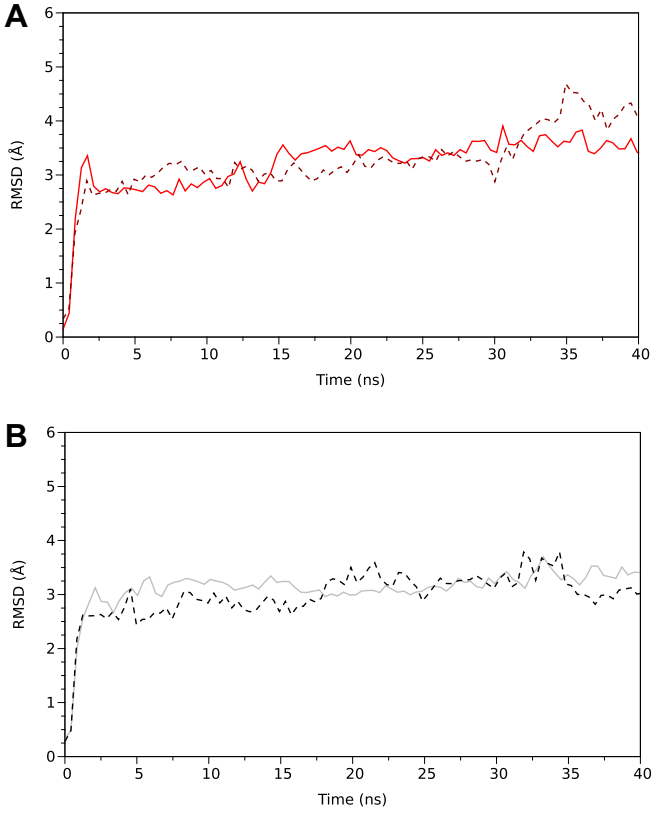


**Fig. 3.** Root-mean-squared deviation from the X-ray structure over simulation time. Red solid line: simulation without TS, run I; dark-red dashed line: simulation without TS, run II; gray solid line: simulation with TS, run I; black dashed line: simulation with TS, run II. Data points smoothed using Bezier curves.

contrast to the individual components, the titration of these complexes (Fig. 2C) with increasing concentrations of TS induced significant changes throughout the CD spectrum, even at 0.1 M equiv of TS, and reached saturation at 1:1:1 stoichiometry of rRNA, protein, and TS. An isosbestic point at 254 nM indicated an apparent 2-state transition, and rules out dilution or medium change effects for this weak, but detectable transition.

### 3.2. Model and simulations stability

Simulation equilibration, general stability, and occurrence of dynamic events were monitored by computing the coordinates' relative deviations from the X-ray input structure as a function of simulation time. Figure 3 shows the RMSD of the protein and rRNA's backbone atoms for all four trajectories. All simulations displayed a prompt, characteristic deviation up to ~3 Å from the input coordinates after removing the restraints. Such RMSD profiles are not unexpected when using a medium-resolution crystal structure as input (3CF5: 3.3 Å),[14] and also represent the structure's local reorganization from the packed solid to the solution phase. After this initial relaxation, the simulations with TS maintains a stable trajectory with RMSD values of $3.2 \pm 0.18$ Å and $3.7 \pm 0.8$ Å. The simulations without TS have a slow, but noticeable, RMSD increase throughout the trajectory, rising from ~2.8 Å to values between 3.4 and 4.0 Å

Based upon the investigations of the RMSD and the radius of gyration over simulation time (see Supplementary Fig. 4) we decided that the production-run data began at 7 and 2.5 ns for the simulations with and without TS. In general, the second simulation runs provide similar data that support our drawn conclusions. For simplicity and clarity we will discuss our results and findings on the basis of the first set of simulations, with exceptions noted.

### 3.3. Large-scale motion

TS binding likely affect L11 · rRNA dynamics and conformations on different time scales and system sizes. PC analysis allows us to investigate the effect that TS binding has on large-scale protein–rRNA conformational changes, which take place on the order of tens of nanoseconds. Thus, data from 7 to 40 ns and from 2.5 to 40 ns for the simulations with and without TS were used for PC analysis, whose results are presented in Figures 4 and 5.

For the simulation without TS, the first three components explain 60% of the complete variance (see Supplementary Fig. 5). The residue-wise loadings for PC1 (Fig. 4D) resemble the overall residue fluctuations (Fig. 6A), suggesting that the NTD contribution dominates this component. Within the NTD, the largest contributions map onto the terminus, the α1 – helix (residues 14–27) and the loop connecting α2 – β2 elements (residues 43–51). Apart

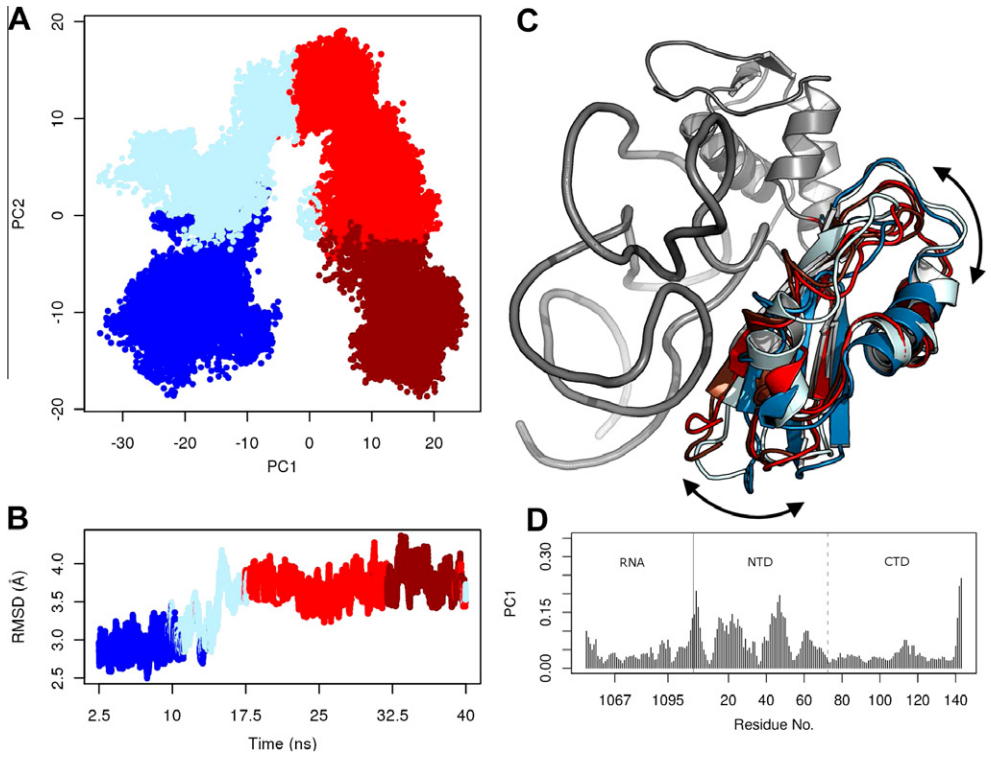


**Fig. 4.** Principal component analysis for the simulation without TS. (A) Clustering in supspace spanned by first three PCs. Clusters 1, 2, 3 and 4 are colored as blue, light-blue, red and dark-red. (B) RMSD plot color-coded according to clusters. (C) Cluster representatives of the NTD, color-coded according to clusters. rRNA and CTD are the ones from cluster representative three. (See Supplementary Fig. 6 A for enlarged structure images.) The motion observed along the first PC is indicated by the arrows. (D) Residue-wise loadings (contributions) in Å to the first PC.

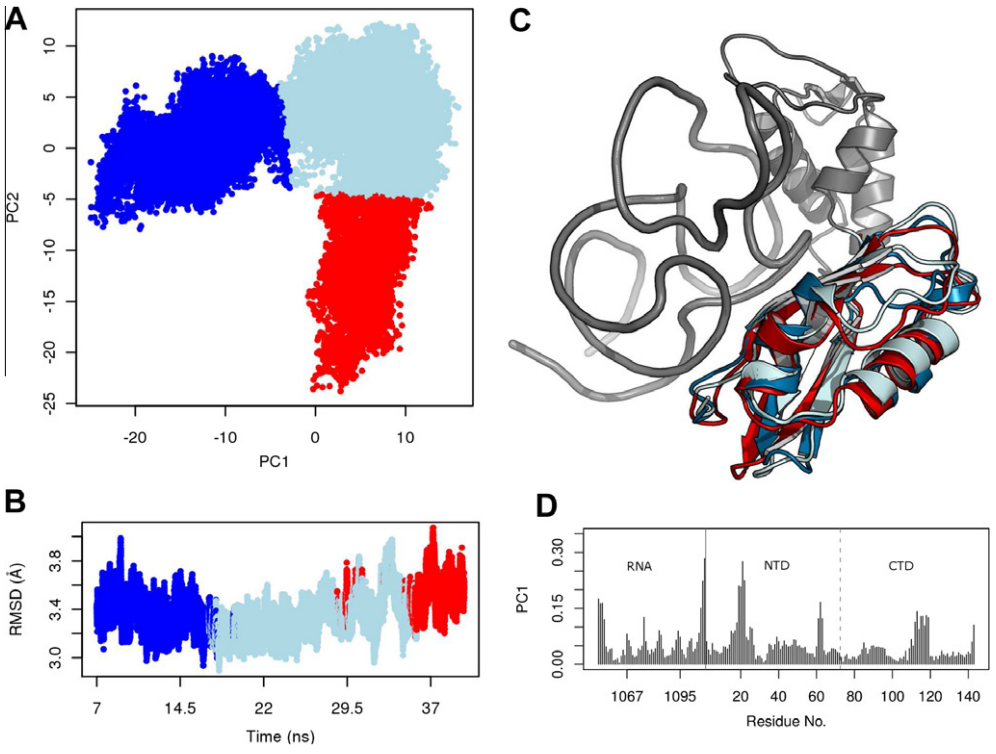


**Fig. 5.** Principal component analysis for the simulation with TS. (A) Clustering in supspace spanned by first three PCs. Clusters 1, 2 and 3 are colored as blue, light-blue and red. (B) RMSD plot color-coded according to clusters. (C) Cluster representatives of the NTD, color-coded according to clusters. rRNA and CTD are the ones from cluster representative two. (See Supplementary Fig. 6B for enlarged structure image.) (D) Residue-wise loadings (contributions) in Å to the first PC.

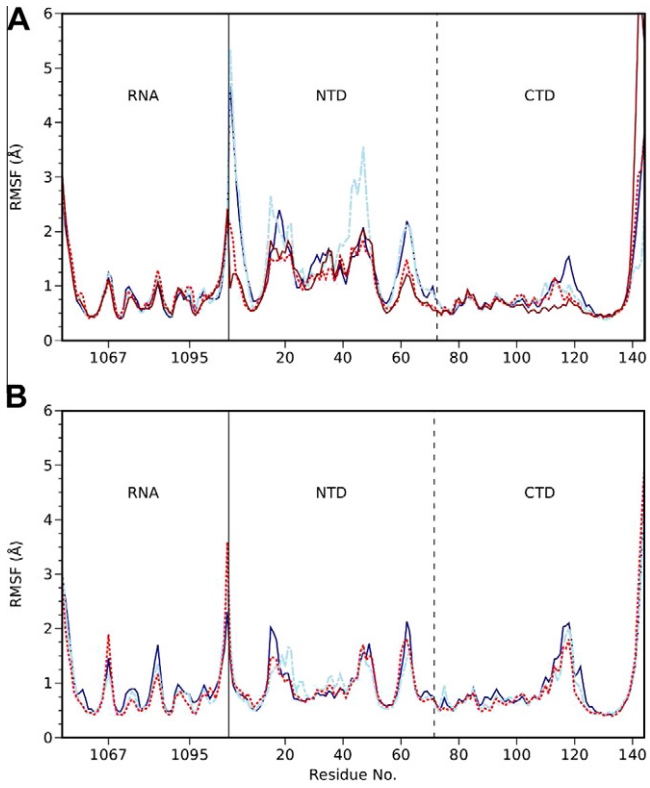


**Fig. 6.** Root-mean-squared fluctuations of residue backbone atoms. (A) Simulation without TS, evaluated at time frames 2.5–10 ns (blue), 10–17.5 ns (light-blue dashed), 17.5–25 ns (red dotted), and 32.5–40 ns (dark-red). (B) Simulation with TS, evaluated at time frames 7–16.5 ns (blue), 16.5–25.5 ns (light-blue dashed), and 25.5–35 ns (red dotted).

from the terminal residues, the CTD and the rRNA contribute little to the motion described by PC1.

The trajectory snapshots clearly form a semicircle, or U-shape, pattern within the PC1 and PC2 projected plane, as seen in Fig. 4A. As Hess pointed out, such a pattern likely indicates random diffusion within the simulation, and interpretable as thermal motion along a relatively flat free-energy landscape.[54,55] While such a result does not inform us of large-scale conformational changes within the system, it does inform us of the more accessible degrees-of-freedom for thermal motion along our investigated time scale.[54]

To compare the conformations sampled during the thermal diffusion, we clustered the trajectory's conformations in the subspace spanned by the first three PCs into four clusters (Fig. 4A and B). The conformational differences between the resulting structural representatives can be described as an NTD rotational movement with respect to the CTD (as indicated by the arrows). Their main differences are in the position of the N-terminus, the nearby loop connecting the $\beta 2--\beta 3$ strands, and the two loops connecting the helices with the $\beta-$ strands at the far end of the NTD's binding site.

The PC analysis of the second run without TS allows similar conclusions to be drawn (Supplementary Fig. 7). The first three PCs, explaining 61% of the overall variance, clearly separate the snapshots into two distinct K-means determined clusters (Supplementary Fig. 7A and B). The representative structures of the two clusters identified in the second simulation align very well with cluster one and three identified in the first simulation (Supplementary Fig. 8). In both sets of clusters, one can clearly see a difference in the NTD orientation relative to the rRNA, validating the observed conformational states. As in the first simulation, the NTD contributes the most to PC1.

**Table 1**
Root-mean-squared deviation (Å) of the NTD's backbone atoms for the PC analysis cluster representatives, using the X-ray[14] conformation as a reference

| | Cluster 1 | Cluster 2 | Cluster 3 | Cluster 4 |
|---|---|---|---|---|
| Simulation without TS | 3.11 | 4.00 | 5.10 | 5.05 |
| Simulation with TS | 4.15 | 4.18 | 4.62 | — |

The first three PC for the trajectory containing TS explains a little less overall variance (48.9%, see Supplementary Fig. 5B). The residue contributions are distributed in a broader manner throughout the L11 · rRNA complex (Fig. 5D). Notable differences occur within the NTD, which form sharp peaks around residues 20 and 62. These residues help form the loops connecting $\beta 1$ to $\alpha 1$ and connecting $\beta 2$ to $\beta 3$. Clustering the conformations in the PC1 to PC3 subspace revealed conformationally similar representatives (Fig. 5C).

The differences between the NTD conformations described by PC1 are further underlined through an RMSD comparison of this domain to the X-ray structure for the different cluster representatives, whose values are seen in Table 1. Whereas the RMSD is nearly the same for all cluster representatives of the simulation with TS ($\Delta$RMSD of 0.5 Å), the RMSD of the first three cluster representatives without TS *each* differ by $\sim$ 1 Å ($\Delta$RMSD of 2.0 Å).

### 3.4. Local residue motion

The dynamic influence that TS has on the L11 · rRNA complex can be investigated by computing each residue's RMSF. Due to our observations in the PC and clustering analysis, we analyzed the obtained clusters separately. We will hereafter consider four equal-length time frames for the simulation without TS (2.5–10 ns, 10–17.5 ns, 17.5–25 ns, and 32.5–40 ns) and three time frames for the simulation with TS (7–16.5 ns, 16.5–25.5 ns, and 25.5–35 ns).

When comparing the RMSF per residue between the two simulations (Fig. 6), the overall pattern is similar, but differences are visible at specific and important positions. The fluctuations within the rRNA and CTD are nearly identical between both simulations with one exception. Within the CTD, the loop (residues 112–122) connecting the $\alpha 4--\alpha 5$ helices shows a consistently high fluctuation when TS is present (Fig. 6B), whereas in the simulation without TS this loop's fluctuation progressively decreases with time (Fig. 6A).

The most notable difference in fluctuations between the two systems occurs in the NTD, where TS's presence stabilizes its dynamics. Particularly noteworthy stabilizations occur in the N-terminus (residues 1–6), $\alpha 1, \alpha 2$, and the turn connecting these two helices (residues 14–48). These differences are most pronounced early in the simulations (blue curves), but are still visible towards the end (red curves) when the fluctuations are drastically reduced in the simulation without TS. Exceptions to the general lower fluctuations observed in the simulation with TS are the consistently high fluctuations around residue 62 in the NTD and a fluctuation increase of the A1067 base, plus the already mentioned loop in the CTD.

### 3.5. rRNA residue conformation

Overall, the rRNA conformation remained fairly compact and immobile throughout all simulations, indicating a stable fold. With the exception of a few nucleotides, all maintained an *anti* base conformation and a C3′-endo puckering. The exceptions are listed in Table 2 and Supplementary Table 2, along with the percentage of base conformation and sugar puckering adopted during both simulations. Of these, the $\chi-$ angle of A1086 and A1088 maintain

**Table 2**
The population percentage of $\chi$ – angle sampled during the simulations with and without TS bound

| | Simulations (without TS \|with TS) | | | X-ray |
|---|---|---|---|---|
| | *Anti* | *High-anti* | *Syn* | |
| A1067 | 4 \| 70 | 3 \| 2 | 93 \| 28 | *Anti* |
| G1068 | 84 \| 99 | 16 \| 1 | 0 \| 0 | *Anti* |
| U1082 | 100 \| 88 | 0 \| 12 | 0 \| 0 | *Anti* |
| C1083 | 100 \| 62 | 0 \| 38 | 0 \| 0 | *Anti* |
| A1084 | 4 \| 4 | 34 \| 75 | 62 \| 21 | *Anti* |
| A1085 | 98 \| 28 | 2 \| 54 | 0 \| 18 | *Anti* |
| A1086 | 2 \| 0 | 0 \| 0 | 98 \|100 | *Syn* |
| G1087 | 35 \| 34 | 64 \| 66 | 1 \| 0 | *Anti* |
| A1088 | 2 \| 0 | 0 \| 0 | 98 \|100 | *Syn* |
| A1095 | 36 \|100 | 27 \| 0 | 37 \| 0 | *Anti* |
| A1096 | 67 \|100 | 33 \| 0 | 0 \| 0 | *Anti* |
| U1097 | 79 \|100 | 21 \| 0 | 0 \| 0 | *Anti* |

The residues listed are either involved in the binding of TS or showed interesting conformational sampling.

their crystal conformation of *syn*, while their linking residue G1087 quickly switches from an *anti* to a stable *high-anti* conformation.

There are three loop apexes within the rRNA that displayed different $\chi$ – angle conformations and dynamic motion that are dependent upon TS's presence. Interestingly, one apex is near the CTD and the loop connecting $\alpha$4 and $\alpha$5 elements, an area that is far from TS's binding cleft. Significant conformational changes were also observed at the apexes of the two helices that participate in TS binding, namely at bases A1067, G1068, A1095, and A1096. Both G1068 and A1096 predominately maintain an *anti* conformation during the simulation with TS, but adopt a small percentage of *high-anti* (16% and 33%) conformation during the simulation without TS. The largest changes are seen in A1067 and A1095, which are the two residues that interact directly with TS. In the simulation with TS, A1067 maintains the crystallographic *anti* conformation for ~ 28 ns, and then samples the *syn* conformation for the remaining time (see $\chi$ – angle in Supplementary Fig. 10 C), which corresponds to the higher fluctuation of this nucleotide at the simulation's end (cmp. Fig. 6). Likewise, A1095 maintains the crystallographic *anti* conformation throughout simulation with TS. However both residues behave differently in the simulation without TS. A1067 quickly adopts a dynamically stable *syn* conformation, while A1095 adopts both *anti* and *high-anti* conformation for ~ 24 ns and then adopts a *syn* conformation for the remaining ~ 16 ns. Note that in the second simulation without TS both nucleotides sample the same $\chi$ – angle conformations but with different lifetimes, with the exception that A1095 does not significantly sample any *anti* or *high-anti* conformation (Supplementary Fig. 10). For both residues a range of sugar puckers are sampled in the simulation without TS, while C3′-endo and C2′-exo are the predominate puckerings in the simulation with TS (see Supplementary Table 2.

### 3.6. Dynamic cross-correlations and protein secondary structure

Dynamic coupling between residues within the L11 · rRNA complex was investigated in both simulations by computing covariance matrices[56] and visualized as dynamic cross-correlation maps (DCCMs). As done in the RMSF analysis, separate DCCMs were computed for each cluster, resulting in the maps shown in Figures 7 and 8. Each DCCM can be separated into three distinct areas, corresponding to rRNA–rRNA, rRNA–protein, and protein–protein cross-correlation.

The percentages of the protein's secondary elements, as computed for each residue, are shown alongside each DCCM. In the simulation without TS, the protein's secondary structure appears to be very stable, with the exception of the NTD's $\alpha$1 and $\alpha$2 – helices. These two secondary elements become more stable in the simulation with TS.

#### 3.6.1. Protein · protein **coupling:**

In nearly all DCCMs shown, the secondary elements within the CTD are positively correlated (Figs. 7 and 8), with minor exceptions occurring within loops and the C-terminus. The motion within the NTD displays both positive and negative correlation when TS is not present, and almost exclusively positive-correlated motion when TS is present. Another general observation is that a coupled movement between the two protein domains exists almost exclusively as anti-correlated motion.

#### 3.6.2. Protein · rRNA **coupling:**

The largest correlations between the protein and rRNA are found in the C-terminal loop connecting $\alpha$3 – –$\beta$4 elements (residues 86–96) with the rRNA residues that form the A1067 apex. This loop makes a significant number of salt bridges and hydrogen bonds to the rRNA,[4] and was shown to undergo an induced fit conformational change upon rRNA binding as revealed by NMR studies.[5] Furthermore, this loop shows very little fluctuations (Fig. 6) and and its local dynamics and conformation are unaffected by TS binding. In general, the C-terminal and rRNA residues that interact through close-range non-bonded interactions are positively correlated, apart from a few anti-correlated residues associated with the protein and rRNA termini. These negatively correlated residues associated with the rRNA termini could be artifacts due to our truncation of the rRNA during our model building. Conversely, the N-terminal and rRNA residues predominately have negative correlation, with the notable reoccurring exception of the positive correlation occurring between A1095 and the $\beta$1 structural element.

#### 3.6.3. rRNA · rRNA **coupling:**

Considering only the nucleic acid structure, positive correlation exists between rRNA residues, with minor exceptions at the terminal residues where the rRNA was artificially truncated for model creation. Consistently occurring in both simulations are two small peaks arising from the interaction of residues near A1067 and A1095. These residues (A1070 and A1096) are part of the rRNA helices that present A1067 and A1095 at their apexes.

#### 3.6.4. [Protein · rRNA] · thiostrepton **coupling:**

The correlated motions of TS with the L11 · rRNA complex is shown in Fig. 8D for the considered time frames. The correlation coefficients between L11 · rRNA's residues and TS (Fig. 8D) range between -0.2 and +0.4, and are thus significantly lower than those observed within the L11 · rRNA biomacromolecule. TS's positive correlation with the N-terminal $\alpha$1 – helix (residues 25–35) is present in all time frames at varying magnitudes, and is probably due to its close spatial proximity to TS. Also notable is that both A1067 and A1095 become positively correlated with TS simulation progresses in time, while the rest of the rRNA becomes anti-correlated (apart from the termini).

## 4. Discussion

#### 4.0.5. Experimental observation

The CD spectral data revealed the influence of TS on the isolated rRNA, the isolated protein species, and the L11 · 23S complex—TS addition did not affect the CD signatures of the isolated components. While minute conformational changes on the single nucleo-

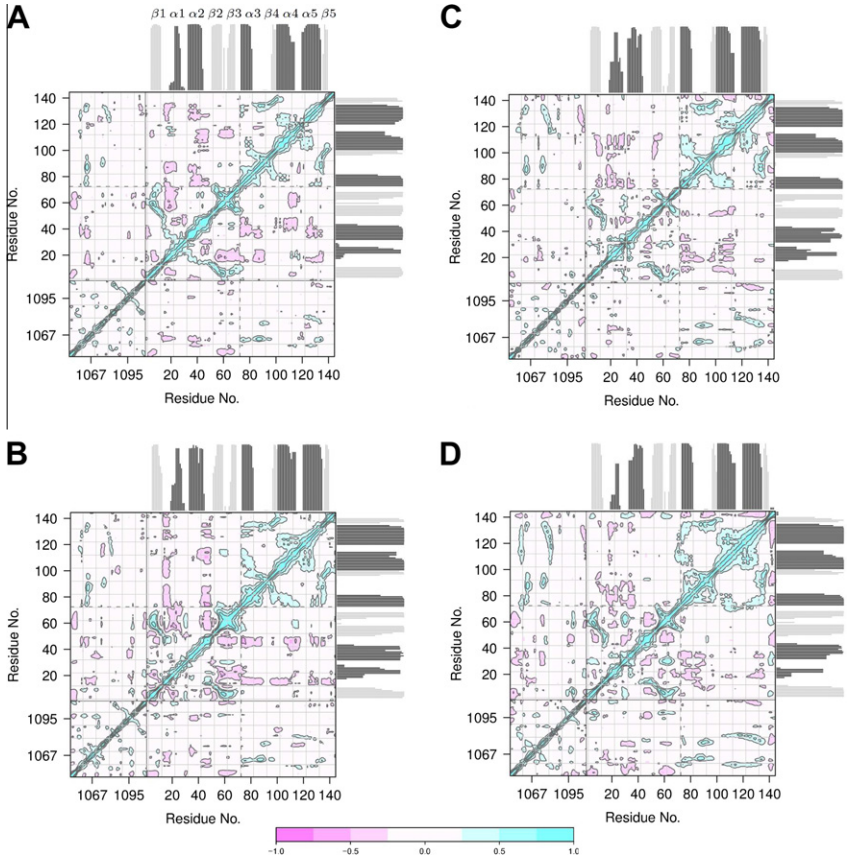


**Fig. 7.** Dynamic cross-correlation maps for the simulation without TS. rRNA and protein residues are divided within the plots using solid black lines, the two protein domains are further divided by dashed gray lines. Cyan colors represent positive correlations, magenta anti-correlations (see color bar at the bottom). The percentage of protein secondary structure occupation during the simulation are displayed by light gray bars (strands) and in dark gray (helices). (A) Analysis performed from 2.5 to 10 ns. (B) Analysis performed from 10 to 17.5 ns. (C) Analysis performed from 17.5 to 25 ns. (D) Analysis performed from 32.5 to 40 ns.

tide level cannot be excluded, as they cannot be resolved by CD spectroscopy, it is very unlikely that stable associations occur in these cases. This implies that TS only affects the conformation of the assembled complex, as indicated by the observed L11 · 23S spectral shift. Because the 265 nm peak characteristic for the rRNA contribution decreased, it could be argued that TS binding has a detectable influence on the 23S conformation in the L11 · 23S complex, potentially by unstacking the 23S nucleobases. The protein component was also affected, as indicated by the characteristic submaximum change at 220 nM, which primarily arises from the protein component. These observations possibly conform to a general tightening of the complex as suggested earlier by other groups.[5,11] Vice versa, the complex should detectably reorganize upon ligand release, and then reach a slightly more A-form-like/ $\alpha$ – helical state.

Based on these critical observations, MD simulations were initiated to provide atomic resolution information on how TS influences the L11 · 23S complex. The ligand-bound state extracted from the X-ray crystal structure of the TS-bound 50S subunit of *D. radiodurans*[14] was chosen as the starting point for computational modeling.

#### 4.0.6. Comparison to previous MD simulation

An all-atom 15 ns MD study of the ribosomal L11 · rRNA subunit, based on a crystal structure of the isolated *Thermotoga maritima* complex (PDB code 1MMS[4]) and without a bound ligand, has been previously reported by Frank and co-worker.[31] While the 1MMS and 3CF5 crystal structures originate from different organisms, were determined in different settings (protein · rRNA complex vs 50S subunit) and the 3CF5 crystal structure resolved an additional ten termini amino acids, we find both similarities and characteristic differences between these data and our simulation without TS bound (Table 3). Foremost, the overall RMSF patterns are comparable, with low and high fluctuations occurring within the C- and N-terminal domains. Especially good RMSF agreement is seen within the rRNA, where five characteristic peaks centered at nucleotides A1067, A1074, A1084, A1095, and C1110 were observed with nearly identical intensities. Our RMSD profile and magnitude (2.5–3.1 Å) is similar to the previous simulation (2–3 Å) for the initial $\sim$ 15 ns, which is the extent the previous simulation was conducted—however, this agreement ended after our simulation underwent a dynamic event at 14.5 ns (see Fig. 4B). We also confirmed Frank and co-worker's observation[31] that A1067 predominately populated the *syn* conformation instead of the crystallographic *anti* conformation.[4,14]

#### 4.0.7. Current MD simulations

Stability and convergence of MD simulations is always a concern when interpreting trajectory data. As shown in the PC analysis projection plot of the simulation without TS and the RMSD plot of the simulation with TS, the simulations do not sample large conformational changes with respect to relative L11 and rRNA domain positions. While observing different stable large-scale conformations, particularly in the simulation without TS, is interesting for a number of reasons, such sampling was not needed in the present investigation. The purpose of this study was to explore if natural

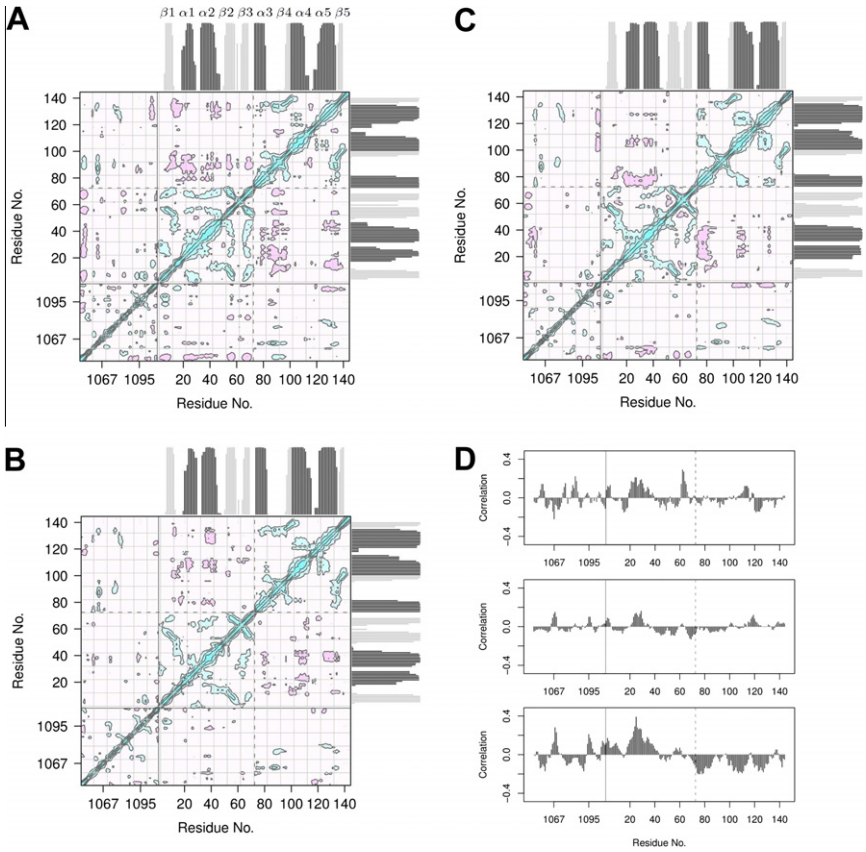


**Fig. 8.** Dynamic cross-correlation maps for the simulation with TS. (A) Analysis performed from 7 to 16.5 ns. (B) Analysis performed from 16.5 to 25.5 ns. (C) Analysis performed from 25.5 to 35 ns. (D) Dynamic correlations of TS with 23S/L11 residues for the time frames analyzed in A, B and C, respectively.

product binding alters local dynamics and the conformations of the 'loose' heterogeneous interfacial L11 · rRNA binding site.

Aside from verifying the sampling of selected torsion angles (data not shown) for convergence, one can separately analyze different time frames within the trajectories to see if the resulting data and drawn conclusions are similar. Our clustering of PC subspace, subsequent projection onto the RMSD plot, and extraction of representative conformations was an attempt to provide a systematic procedure for generating these different time frames. For the observables measured herein, we see sufficient sampling (e.g., $\chi$ – angles) and general convergence in data (e.g., DCCM, protein secondary structure) between the different time frames for each model simulation.

In the simulations without TS, the PC analysis revealed a significant amount of thermal diffusion by the L11 · rRNA backbone atoms. An overlay of the simulation's macromolecular representative structures (Fig. 4C) and and PC animation (data not shown) revealed that this thermal motion primarily resides within the NTD. Thus, it appears that the free energy surface for this local movement is relatively flat and accessible at body temperature.[54,55] Further support of this localized motion comes from the RMSD data, where a small dynamic event takes place during the simulation that raises the RMSD by an additional 1 Å (Fig. 4B).[1] Large-scale protein flexibility within the ligand free L11 · rRNA has previously been found in experimental structural studies, accompanied by the suggestion that the L11 protein can adopt 'bound' and 'unbound' conformations.[57,5,14] These experimental studies, which presumably sample long time scales motion (i.e., $\geqslant \mu s$), and our MD simulations collectively support the idea that significant NTD motion exists when a natural product is not bound.

In the simulations with TS, the distribution of conformational snapshots in the PC subspace supported three clusters. However, these clusters are very similar to one another, as shown in the color-coded RMSD plot and the overlay of their representatives structures (Fig. 5B and C). Most of the differences reside in the loop structure connecting α1 to α2. With regard to the binding cleft characterization, one macromolecular conformation is essentially sampled throughout the simulation. The presence of TS clearly stabilizes L11 · rRNA thermal motion, restricting the NTD motion of the local 'ligand-free' free energy surface.

The dynamic effect that TS binding exerts on residues within the system's separate subdomains (i.e., rRNA, CTD and NTD) was investigated by computing residue-wise RMSF and dynamic cross-correlation maps (DCCMs). In each of the simulations (with and without TS), the rRNA residues had little fluctuations, apart from a few small prominent peaks (Fig. 6). Similarly, the CTD residues displays low fluctuation apart from a prominent peak occurring in the loop (residues 112–122) connecting the α4-α5 helices, which decreases as the simulation progresses. For the simulation without TS, the NTD residues shows the greatest fluctuations in the L11 · rRNA.

Thiostrepton binding has a significant impact on the residue dynamics within the protein domains. The overall RMSF within the NTD is reduced, while leaving three loop structures with high fluctuations relative to the other amino acids. Surprisingly, there is an increase in fluctuations around the loop (residues 112–122) connecting the C-terminal's α4 – α5 helices. This loop makes direct contacts to the rRNA and the NTD of the ribosomal protein L10 within the assembled 50S subunit.[2,3] Hypothetically, when in the presence of L10 this conformational transmission may become

[1] A similar RMSD increase occurs in the second L11 · rRNA simulation, but at a later time period.

**Table 3**
Root-mean-squared deviation (Å) between simulation cluster representatives and available crystal structures 3CF5 and 1MMS[a]

| | 1MMS | Simulation without TS | | | | Simulation with TS | | |
|---|---|---|---|---|---|---|---|---|
| | | 1 | 2 | 3 | 4 | 1 | 2 | 3 |
| 3CF5 | 2.0 \|2.3 | 2.3 \|2.7 | 2.5 \|3.3 | 2.9 \|4.2 | 3.0 \|4.5 | 2.7 \|3.2 | 2.7 \|3.3 | 3.0 \|4.0 |
| 1MMS | — | 1.8 \|2.4 | 2.0 \|3.1 | 2.1 \|3.0 | 2.1 \|3.1 | 2.0 \|2.2 | 2.0 \|2.2 | 2.3 \|2.9 |

Backbone RMSD |NTD RMSD (with fitting to complete backbone).
[a] Only residues common to all structures were considered, that is, nucleotides 1051–1108 for 23S rRNA, and residues 7–139 for L11.

more pronounced and could productively contribute to a hinge-like motion of the GAR, potentially coupling EF-G and TS binding to the L7/L12 stalk. Stabilization of the protein's secondary structures is also observed upon TS binding, particularly with the $\alpha 1-$ helix (Fig. 8A–D). In the ligand-free state, the residues composing this helix have significant dynamic motion over all time periods sampled—causing disorder to occur within the secondary element (Fig. 7A–D).

Determining the cross-correlation coefficients between the residue motions provided understanding into the collective motion within the L11 · rRNA complex, revealing the dynamic relationships between residues, secondary structure elements, and domains. Without a bound ligand, the motions between the C- and N-terminal domains are predominately anti-correlated. Within the CTD, positive correlation dominates the motion, and the same is true within the rRNA structure. The motion between the rRNA and CTD is predominately positively correlated, while between the rRNA and NTD the motion is nearly all anti-correlated. However, a reproducible complex coupling of both negatively and positively correlated motions characterizes the NTD when TS is absent.

In the presence of TS, the overall correlated motion of the L11 · rRNA macromolecule is reduced (Fig. 8). The concerted motion between the C- and N-terminal domains loose their weak positive correlation, and become entirely anti-correlated. There is also little effect on the correlated motion within the rRNA, upon ligand binding. The most significant change occurs in the correlated motion within each protein domain where they become entirely positively correlated, which is especially pronounced within the NTD. The correlated motion between each of the protein domains with the rRNA is also noticeably reduced. Furthermore, the motion between TS and A1067 and A1095 are slightly positively correlated (Fig. 8D). Consistently throughout the simulation, TS's motion is positively correlated with the $\alpha 1-$ helix, which itself shows correlation with various other secondary elements in both the C- and N-terminal domains.

On the local level TS clearly effect the conformations of nearby residues, especially prominent in an altered A1067 and A1095 $\chi-$ angle preference and increased $\alpha 1-$ helix stability. The exposed nucleobase A1067 has been assigned multifunctional roles in tRNA and elongation factor recognition.[31,3,13] Both *syn* and *anti* conformations of its $\chi-$ angle were sampled during a simulation by Frank and co-workers in the absence of a ligand. [31] Our simulation without TS confirms this property, but we find a stronger *syn* preference. In contrast to their finding, we observed A1067's $\chi-$ angle fluctuations throughout the trajectory (see Supplementary Fig. 10A), and found no correlation between its conformation and the N-terminal loop movements that connects the $\beta 2-\beta 3$ strands. Interestingly, in the simulation containing TS this $\chi-$ angle is strongly positioned in an *anti* conformation ($187 \pm 10^{\circ}$) for $\sim 27$ ns, and aligns well with the value observed by X-ray crystallography ($174^{\circ}$). TS clearly stabilizes A1067's *anti* conformation, but does not entirely inhibit the nucleobase from adopting a *syn* conformation. This base-flipping event is preceded by a loss of the hydrogen bond formed between an amide group of TS's macrocycle A and N3 of A1067, whose presence probably fixes the base in the *anti* conformation (see Supplementary Fig. 11A). Instead, we see the formation of a hydrogen bond to N7 at the opposite side of the base, stabilizing the *syn* conformation sampled later in the simulation (Supplementary Fig. 11B). Furthermore, A1095 samples *anti*, *high-anti*, and *syn* conformations when TS is not present, but only the *anti* conformation when TS is bound.

Due to the implicated importance of these residues to TS binding, we performed two additional simulations for validation—one on an adenosine monomer and the other on a trimer. The $\chi-$ angles observed during these two simulations are shown in Supplementary Fig. 12. In the adenosine monomer simulation, the *syn* preference was reproduced. However, the preference shifted to the *high-anti* conformation when flanked on each side by an additional adenosines (trimer). This suggests that A1067's base is sterically unhindered by its surrounding environment in the absence of TS. To a lesser extent, TS appears to also influence the base orientations of U1082, C1083, A1084, and A1085, which are located near the protein's CTD. As a caveat, it cannot be completely ruled out that the preference for *high-anti* over *anti* conformations we observed for some nucleobases is due to parameterization error within the Parm99SB and Parmbsc0 force fields.[58,59]

A previous computational study of allowed conformations in nucleic acid monomers indicated that the adenosine $\chi-$ angle preferentially adopts a *syn* conformation with a C2′-endo sugar pucker, and to a lesser extent when the sugar puckering is C3′-endo.[60] The *anti* conformation is populated when the sugar puckering is either C2′- or C3′-endo. Consistent with this notion, we found the C2′-endo (50%) and closely related C1′-exo (20%) to be the predominant conformations for A1067's ribose in the simulation without ligand (Table S1), and its base had a strong *syn* $\chi-$ angle preference (Table 2). However, when TS is bound, A1067's ribose preferentially adopts the C3′-endo (42%) and C2′-exo (29%) conformations, along with a *high-anti* population of the $\chi-$ angle. The A1095 sugar populates several puckerings—C2′-exo (38%), C1′-endo (17%), C2′-endo (14%), C1′-exo (12%), and C3′-endo (8%)—when TS is not present, coinciding with diverse sampling of its $\chi-$ angle. When TS is bound, the puckering predominately becomes C2′-exo (66%) and C3′-endo (31%), along with its *anti* $\chi-$ angle.

Within the ribosome a strong propensity for antibiotic binding sites to locate at non-paired bases, at *syn*-configured RNA bases, and at C2′-endo and C4′-exo sugar pucker sites was found. [61] A1067's conformational parameters conform to these general properties of ribosomal ligand binding sites. However, the binding site reorganizes when TS is bound. Since the actual binding event cannot be simulated for such a large system without inappropriate simplification, it remains unclear if this reorganization takes place during or after the ligand binding. This switch-like conformational reprogramming of A1067 and its surroundings might be an important part of the molecular activity of the thiopeptides. This property might also relate to the observed resistance pattern and specific mutations, which allow protein biosynthesis to proceed while TS is bound.[15] Furthermore, the natural mechanism of self-resistance features a crucial methylation of the 2'OH group at A1067. Beyond the breaking of apparent hydrogen bond network within the binding site, [62] this modification could drive the conformational prefer-

ences of A1067 toward a state unreceptive for thiostrepton binding, potentially by indirectly modulating the sugar pucker and/or the *syn*/*anti* preference of the projected nucleobases.[63,64]

## 5. Conclusion

By embedding all components of the ternary L11 · rRNA · TS ribosomal complex in an all-atom solvated MD simulation, a truncated computational model of the binding environment and the local dynamics of the GAR was created. Starting from an X-ray crystal structure of the ligand-bound state[14] an advanced and highly integrated target model was realized. We found, that TS binding locally rigidifies the thiopeptide binding area on the L11 protein and characteristically reprograms the conformation of the apical nucleotide A1067, which mediates contacts to tRNA and incoming ribosomal factors. Otherwise, rRNA conformation is not detectably affected by TS binding. Removing TS from the L11 · rRNA complex, immersing it in solvent, and heating it to room temperature resulted in significant thermal motion of the NTD with respect to the CTD and rRNA. In the presence of TS, the overall dynamic motions and correlations thereof of the L11 · rRNA complex became more stable. Principal component and dynamic cross correlation analyses of TS bound and unbound states located regions of fold change and of coupled motions.

These results align with CD spectroscopy data, which clearly showed a two-state transition of the protein–rRNA complex upon ligand binding. However, the ligand-free CD-spectrum of the L11 · rRNA complex likely includes additional conformational states which have not been sampled by our MD trajectories. In the ribosomal X-ray crystallography work, a shift in the distal portion of L11 (i.e., N-terminus and Glu62 turn) was noted when comparing the unbound and TS-bound form.[14]

Considering the energetics of ligand binding, a balance must exist between the binding enthalpy of the ligand and the entropy increase or decrease that occurs across the entire target and in the solvation shell. On the one hand, the NTD gains an entropy decrease due to stabilization in its residue fluctuations, while on the other hand it has an entropy increase due to a reduction of overall correlated motions. The design and optimization of new inhibitors of the GAR will likely need to take both the binding enthalpy and the resulting entropy effects on the L11 · rRNA macromolecule into account. The data presented herein should aid this process by having identified crucial properties of the complex target, and provide a validated model basis for ligand discovery strategies in silico.

## Acknowledgments

We thank Dr. Astrid Maaß, Dr. Dirk Reith, and Professor Dr. Martin Hofmann-Apitius for helpful discussions throughout the execution of this research, and Professor Barry Grant for assistance with the bio3d package.

## Supplementary data

Supplementary data associated with this article can be found, in the online version, at http://dx.doi.org/10.1016/j.bmc.2012.09.025.

## References

1. Mohr, D.; Wintermeyer, W.; Rodnina, M. V. *Biochemistry* **2002**, *41*, 12520.
2. Diaconu, M.; Kothe, U.; Schlünzen, F.; Fischer, N.; Harms, J. M.; Tonevitsky, A. G.; Stark, H.; Rodnina, M. V.; Wahl, M. C. *Cell* **2005**, *121*, 991.
3. Gao, Y.-G.; Selmer, M.; Dunham, C. M.; Weixlbaumer, A.; Kelley, A. C.; Ramakrishnan, V. *Science* **2009**, *326*, 694.
4. Wimberly, B. T.; Guymon, R.; McCutcheon, J. P.; White, S. W.; Ramakrishnan, V. *Cell* **1999**, *97*, 491.
5. Jonker, H. R. A.; Ilin, S.; Grimm, S. K.; Wöhnert, J.; Schwalbe, H. *Nucleic Acids Res.* **2007**, *35*, 441.
6. Wilson, D. N.; Nierhaus, K. H. *Crit. Rev. Biochem. Mol. Biol.* **2005**, *40*, 243.
7. Donovick, R.; Pagano, J. F.; Stout, H. A.; Weinstein, M. J. *Antibiot. Annu.* **1955**, *3*, 554.
8. Dutcher, J. D.; Vandeputte, J. *Antibiot. Annu.* **1955**, *3*, 560.
9. Rosendahl, G.; Douthwaite, S. *Nucleic Acids Res.* **1994**, *22*, 357.
10. Porse, B. T.; Leviev, I.; Mankin, A. S.; Garrett, R. A. *J. Mol. Biol.* **1998**, *276*, 391.
11. Bowen, W. S.; Dyke, N. V.; Murgola, E. J.; Lodmell, J. S.; Hill, W. E. *J. Biol. Chem.* **2005**, *280*, 2934.
12. Baumann, S.; Schoof, S.; Harkal, S. D.; Arndt, H.-D. *J. Am. Chem. Soc.* **2008**, *130*, 5664.
13. Walter, J. D.; Hunter, M.; Cobb, M.; Traeger, G.; Spiegel, P. C. *Nucleic Acids Res.* **2012**, *40*, 360.
14. Harms, J. M.; Wilson, D. N.; Schlünzen, F.; Connell, S. R.; Stachelhaus, T.; Zaborowska, Z.; Spahn, C. M. T.; Fucini, P. *Mol. Cell* **2008**, *30*, 26.
15. Baumann, S.; Schoof, S.; Bolten, M.; Haering, C.; Takagi, M.; Shin-ya, K.; Arndt, H.-D. *J. Am. Chem. Soc.* **2010**, *132*, 6973.
16. *Computational studies of RNA and DNA*; Šponer, J., Lankas, F., Eds.; Springer: Dordrecht, 2006.
17. McDowell, S. E.; Spacková, N.; Šponer, J.; Walters, N. G. *Biopolymers* **2007**, *85*, 169.
18. Ditzler, M. A.; Otyepka, M.; Šponer, J.; Walter, N. G. *Acc. Chem. Res.* **2010**, *43*, 40.
19. Wang, Y.; Shen, J. K.; Schroeder, S. J. *J. Phys. Chem. Lett.* **2012**, *3*, 1007.
20. Rázga, F.; Koca, J.; Šponer, J.; Leontis, N. B. *Biophys. J.* **2005**, *88*, 3466.
21. Rázga, F.; Zacharias, M.; Réblová, K.; Koca, J.; Šponer, J. *Structure* **2006**, *14*, 825.
22. Réblová, K.; Rázga, F.; Li, W.; Gao, H.; Frank, J.; Šponer, J. *Nucleic Acids Res.* **2010**, *38*, 1325.
23. Rázga, F.; Koca, J.; Mokdad, A.; Šponer, J. *Nucleic Acids Res.* **2007**, *35*, 4007.
24. Besseová, I.; Réblová, K.; Leontis, N. B.; Šponer, J. *Nucleic Acids Res.* **2010**, *38*, 6247.
25. Whitford, P. C.; Onuchic, J. N.; Sanbonmatsu, K. Y. *J. Am. Chem. Soc.* **2010**, *132*, 13170.
26. Trylska, J.; Tozzini, V.; McCammon, J. A. *Biophys. J.* **2005**, *89*, 1455.
27. Sanbonmatsu, K. Y.; Joseph, S. *J. Mol. Biol.* **2003**, *328*, 33.
28. Sanbonmatsu, K. Y.; Joseph, S.; Tung, C.-S. *Proc. Natl. Acad. Sci. U.S.A.* **2005**, *102*, 15854.
29. Li, W.; Ma, B.; Shapiro, B. *J. Biomol. Struct. Dyn.* **2001**, *19*, 381.
30. Li, W.; Ma, B.; Shapiro, B. A. *Nucleic Acids Res.* **2003**, *31*, 629.
31. Li, W.; Sengupta, J.; Rath, B. K.; Frank, J. *RNA* **2006**, *12*, 1240.
32. Réblová, K.; Spacková, N.; Koca, J.; Leontis, N. B.; Šponer, J. *Biophys. J.* **2004**, *87*, 3397.
33. E. Gasteiger, C. Hoogland, A. Gattiker, S. Duvaud, M.R. Wilkins, R. Appel, A. Bairoch, in: J.M. Walker (Ed.), The Proteomics Protocols Handbook, Humana Press, 2005, pp. 571–607.
34. Schoof, S.; Baumann, S.; Ellinger, B.; Arndt, H.-D. *ChemBioChem* **2009**, *10*, 242.
35. Case, D. A.; Darden, T. A.; Cheatham, T. E. III; Simmerling, C. L.; Wang, J.; Duke, R. E.; Luo, R.; Walker, R. C.; Zhang, W.; Merz, B. Roberts, K. M.; Wang, B.; Hayik, S.; Roitberg, A.; Seabra, G.; Kolossváry, I.; Wong, K. F.; Paesani, F.; Vanicek, J.; Liu, J.; Wu, X.; Brozell, S. R.; Steinbrecher, T.; Gohlke, H.; Cai, Q.; Ye, X.; Wang, J.; Hsieh, M. -J.; Cui, G.; Roe, D. R.; Mathews, D. H.; Seetin, M. G.; Sagui, C.; Babin, V.; Luchko, T.; Gusarov, S.; Kovalenko, A.; Kollman, P. A. AMBER 11, http://www.ambermd.org, 2010. University of California, San Francisco
36. Hornak, V.; Abel, R.; Okur, A.; Strockbine, B.; Roitberg, A.; Simmerling, C. *Proteins* **2006**, *65*, 712.
37. Pérez, A.; Marchán, I.; Svozil, D.; Šponer, J.; Cheatham, T. E.; Laughton, C. A.; Orozco, M. *Biophys. J.* **2007**, *92*, 3817.
38. Bond, C. S.; Shaw, M. P.; Alphey, M. S.; Hunter, W. N. *Acta Crystallogr. D* **2001**, *57*, 755.
39. Wang, J.; Wolf, R. M.; Caldwell, J. W.; Kollman, P. A.; Case, D. A. *J. Comput. Chem.* **2004**, *25*, 1157.
40. Breneman, C. M.; Wiberg, K. B. *J. Comput. Chem.* **1990**, *11*, 361.
41. Wang, J.; Cieplak, P.; Kollman, P. A. *J. Comput. Chem.* **2000**, *21*, 1049.
42. Gordon, M. S.; Schmidt, M. W. In *Theory and Applications of Computational Chemistry: the First Forty Years*; Gordon, M. S., Schmidt, M. W., Dykstra, C. E., Eds.; Elsevier: Amsterdam, Boston, 2005; pp 1167–1189.
43. Jorgensen, W. L.; Chandrasekhar, J.; Madura, J. D.; Impey, R. W.; Klein, M. L. *J. Chem. Phys.* **1983**, *79*, 926.
44. Essmann, U.; Perera, L.; Berkowitz, M. L.; Darden, T.; Lee, H.; Pedersen, L. G. *J. Chem. Phys.* **1995**, *103*, 8577.
45. Ryckaert, J.-P.; Ciccotti, G.; Berendsen, H. *J. Comput. Phys.* **1977**, *23*, 327.
46. Team, R. D. C. *R: A Language and Environment for Statistical Computing*; R Foundation for Statistical Computing: Vienna, Austria, 2009.
47. Amadei, A.; Linssen, A. B.; Berendsen, H. J. *Proteins* **1993**, *17*, 412.
48. Hayward, S.; de Groot, B. L. *Methods Mol. Biol.* **2008**, *443*, 89.
49. Grant, B. J.; Rodrigues, A. P. C.; ElSawy, K. M.; McCammon, J. A.; Caves, L. S. D. *Bioinformatics* **2006**, *22*, 2695.
50. Wolf, A.; Kirschner, K. N. *J. Mol. Mod.* **2012**. http://dx.doi.org/10.1007/s00894-012-1563-4.
51. Kabsch, W.; Sander, C. *Biopolymers* **1983**, *22*, 2577.
52. Altona, C.; Sundaralingam, M. *J. Am. Chem. Soc.* **1972**, *94*, 8205.
53. G.D. Fasman, Circular Dichroism and the Conformational Analysis of Biomolecules., Plenum Press, New York, 1996.
54. Hess, B. *Phys. Rev. E* **2000**, *62*, 8438.
55. Hess, B. *Phys. Rev. E* **2002**, *65*, 031910.
56. Ichiye, T.; Karplus, M. *Proteins* **1991**, *11*, 205.

57. Lee, D.; Walsh, J. D.; Yu, P.; Markus, M. A.; Choli-Papadopoulou, T.; Schwieters, C. D.; Krueger, S.; Draper, D. E.; Wang, Y.-X. *J. Mol. Biol.* **2007**, *367*, 1007.
58. Zgarbová, M.; Otyepka, M.; Šponer, J.; Mládek, A.; Banás, P.; Cheatham, T. E., III; Jurecka, P. *J. Chem. Theory Comput.* **2011**, *7*, 2886.
59. Sklenovský, P.; Florová, P.; Banás, P.; Réblová, K.; Lankas, F.; Otyepka, M.; Šponer, J. *J. Chem. Theory Comput.* **2011**, *7*, 2963.
60. Yildirim, I.; Stern, H. A.; Kennedy, S. D.; Tubbs, J. D.; Turner, D. H. *J. Chem. Theory Comput.* **2010**, *6*, 1520.
61. David-Eden, H.; Mankin, A. S.; Mandel-Gutfreund, Y. *Nucleic Acids Res.* **2010**, *38*, 5982.
62. Jonker, H. R. A.; Baumann, S.; Wolf, A.; Schoof, S.; Hiller, F.; Schulte, K. W.; Kirschner, K. N.; Schwalbe, H.; Arndt, H.-D. *Angew. Chem. Int. Ed.* **2011**, *50*, 3308.
63. Kawai, G.; Ue, H.; Yasuda, M.; Sakamoto, K.; Hashizume, T.; McCloskey, J. A.; Miyazawa, T.; Yokoyama, S. *Nucleic Acids Symp. Ser.* **1991**, *25*, 49.
64. Kawai, G.; Yamamoto, Y.; Kamimura, T.; Masegi, T.; Sekine, M.; Hata, T.; Iimori, T.; Watanabe, T.; Miyazawa, T.; Yokoyama, S. *Biochemistry* **1992**, *31*, 1040.